IEEE Photonics Journal
An IEEE Photonics Society Publication

Open Access

Phase Calibration of On-Chip Optical Phased Arrays via Interference Technique

Volume 12, Number 2, April 2020

Haiyang Zhang
Zixuan Zhang
Chao Peng
Weiwei Hu

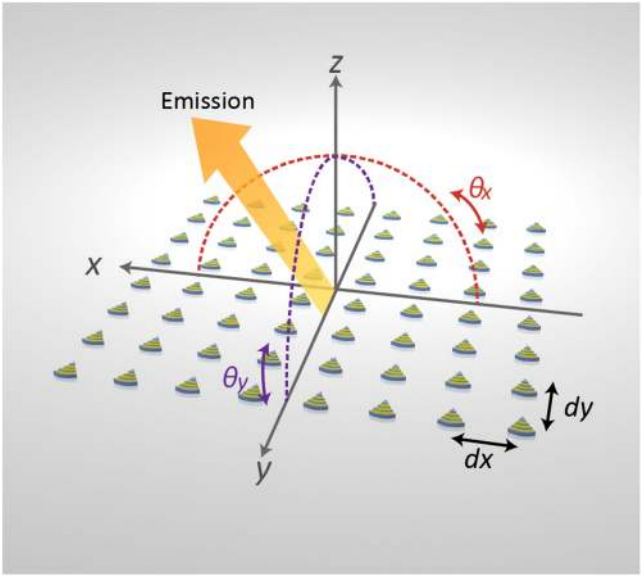

DOI: 10.1109/JPHOT.2020.2968002

Phase Calibration of On-Chip Optical Phased Arrays via Interference Technique

Haiyang Zhang, Zixuan Zhang, Chao Peng, and Weiwei Hu

State Key Laboratory of Advanced Optical Communication Systems and Networks, Department of Electronics, Peking University, Beijing 100871, China

DOI:10.1109/JPHOT.2020.2968002

Manuscript received December 2, 2019; revised December 30, 2019; accepted January 16, 2020. Date of publication January 20, 2020; date of current version March 3, 2020. This work was supported in part by the National Key Research and the Development Project of China under Grant 2018YFB2201704, in part by the National Natural Science Foundation of China under Grant 61575004, and in part by the State Key Laboratory of Advanced Optical Communication Systems and Networks, China. Corresponding author: Chao Peng (e-mail: pengchao@pku.edu.cn).

Abstract: Optical phased arrays (OPAs) are promising in various applications owing to their excellent beam steering performance but suffer from the random initial phases ruining the beam patterns. In this work, an interference-based calibration method to align the random phases for OPA operations is proposed. Briefly, the phase differences are directly extracted from the interference fringes and used to build up the phase map. The feasibility and effectiveness of the proposed method were verified from an 8×8 OPA chip, in which the side-lobe suppression ratio of 10.1 dB was achieved. The proposed method can be utilized as a supplement of conventional calibration algorithms to reduce requirements for the sensitivity of the feedback system and avoid local optima, thus providing practical assistance for many OPA applications.

Index Terms: Optical phased array, phase calibration, integrated optics.

1. Introduction

Owing to the promising potentials in beam steering and formation, optical phased arrays (OPAs) have attracted widespread attention in recent decades [1]–[3], particularly in those burgeoning fields of light detection and ranging (LiDAR) [4], [5], three-dimensional (3D) projection [6], [7], and optical wireless communications [8]. Several types of OPA, such as liquid crystals [9]–[12], reflective optical microelectromechanical systems (MEMS) [13]–[15], and laser arrays [16]–[19] have been proposed and demonstrated.

In principle, the desired far-field beam patterns of OPAs are realized by manipulating the phases of the emissions from each of the antennas. To promote the beam steering performance, the antenna layout should be in a wavelength-level scale, and hence, high-density on-chip integration technologies are indispensable for achieving larger-scale OPAs. Thanks to the rapid development of silicon photonics, OPAs on silicon-on-insulator (SOI) platform has shown many advantages in the compact size, low power consumption, and fast operation speed [20]–[24], which makes it a promising candidate for high-resolution spatial beamformer compared with those conventional liquid crystal solutions [25]–[31].

However, due to the fabrication imperfections, there inevitably exist length differences of the light paths when connecting their antennas. As a result, random distributed but temporally constant initial phases will be induced and may destroy the desired far-field patterns if an appropriated

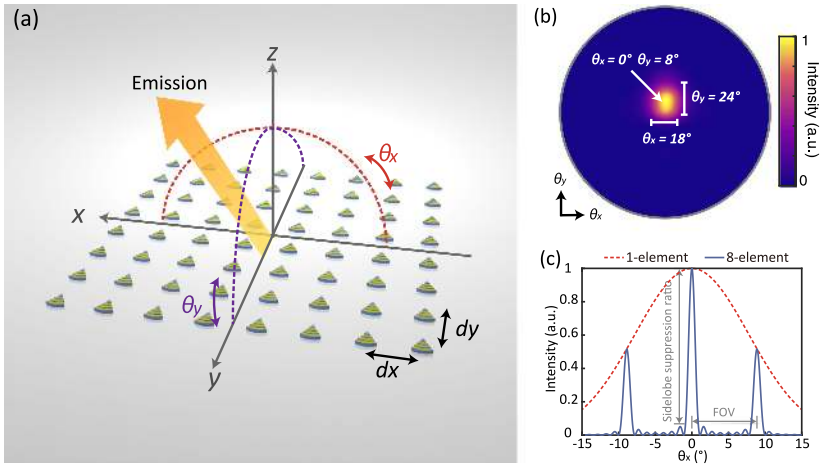

Fig. 1. (a) Schematic of the 2D antenna array. (b) Far-field pattern of one antenna. (c) Far-field patterns of a 1D array with 1 or 8 elements at the antenna spacing of 10 μm.

phase calibration is absent. In order to achieve the ideal beam steering, it is essential to align chaotic initial phases into regular ones, and conventionally, this is done by using mathematical algorithms [32]–[36], such as the stochastic parallel gradient descent (SPGD). In the SPGD algorithm, the effectiveness of the optimization is judged by a fitness function, which decides the most suitable gradient and iteratively directs the optimization.

In general, since the side lobes is relatively low to be exactly recognized, it is difficult and time-consuming to found a proper and precise fitness function, especially for the calibration of large-scale two-dimensional (2D) on-chip OPA configurations. Besides, due to the nonlinear dependence between the initial phases and far-field pattern, the algorithms usually encounter difficulties in being trapped into local optima. Hence, they either cannot find the exact optimum to operate the OPAs in the best setting, or need more efforts to solve convergence problems.

In this work, we propose an interference technique to physically calibrate the initial phases of the OPA, in order to overcome the mathematical difficulties of conventional algorithm-based calibration methods. Briefly, the phase difference between two adjacent antennas was measured directly through their interference fringes in the far field. By progressively repeating this procedure for different columns and rows of the antenna array, a look-up table (LUT) of the initial phases was generated and ready for driving the OPA to form a stared beam pattern. The effectiveness of the interference-based calibration method was verified on a silicon-based OPA with a scale of 8 $\times$ 8 elements, and a side-lobe suppression ratio of 10.1 dB was achieved.

The remainder of this paper is organized as follows. Section 2 describes the theory and derivations of the interference-based calibration method. Section 3 present the optical setup and the measured results of the calibration. Finally, we raise some discussions in Section 4 and conclude our work in Section 5.

2. Theory of Interference-Based Calibration

In this section, we derive the theory of the interference-based calibration method. The schematic of an antenna array with 2D configuration is shown in Fig. 1(a), in which the antennas located in the $x-y$ plane emit the beams to free space individually. The phases of emission beams are manipulated by a series of phase shifters. For an M $\times$ N OPA, the far-field beam pattern $U(\theta_x, \theta_y)$ is the Fourier transform of the near-field waveform $E(x, y)$, which follows:

$$U(\theta_x, \theta_y) = F(E(x, y)) = \iint_{-\infty}^{\infty} E(x, y) \cdot e^{-i\frac{2\pi}{\lambda}(x \sin\theta_x + y \sin\theta_y)} dxdy, \quad (1)$$

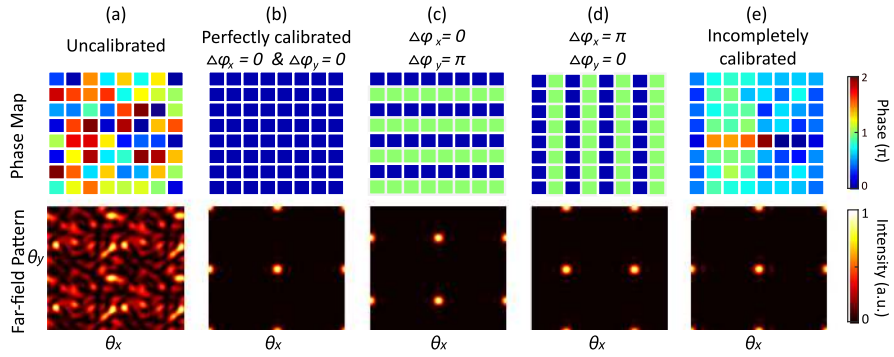

Fig. 2. (a) Randomly distributed and (b)–(d) calibrated phases for the 8 × 8 antenna array and the far-field patterns accordingly. (e) Incompletely calibrated phases, or called local optima of the calibration and its far-field pattern. The field-of-views are centered to the diffraction center of single antenna.

where λ is the free-space wavelength, and θ_x and θ_y represent the far-field angles in two directions. For such uniformly arranged OPA, the antenna spacing in the x and y directions are given as d_x and d_y, respectively. Therefore, the near-field waveform can be depicted by a set of 2D discrete values:

$$E(x, y) = \sum_{m=1}^{M} \sum_{n=1}^{N} a_{mn} \cdot e^{i\phi_{mn}} \cdot \delta(x - md_x, y - nd_y), \tag{2}$$

where a_{mn} and ϕ_{mn} are the amplitude and phase of single emission in the m_{th} row and the n_{th} column, respectively. Assume all the antennas are identical, we combine Eq. (1) with Eq. (2) and obtain $U(\theta_x, \theta_y)$ as

$$U(\theta_x, \theta_y) = A(\theta_x, \theta_y) \cdot \sum_{m=1}^{M} \sum_{n=1}^{N} e^{-i\frac{2\pi}{\lambda}(md_x \sin\theta_x + nd_y \sin\theta_y) + i\phi_{mn}}, \tag{3}$$

where $A(\theta_x, \theta_y)$ is the far-field waveform of single emission determined by the single antenna design. However, ϕ_{mn} – namely the phases of the emissions from each of the antennas, is not necessarily identical, because the design and fabrication would induce randomly disordered but temporal steady initial phases. As a result, the far-field pattern is quite chaotic, as shown in Fig. 2(a), and thus ϕ_{mn} have to be calibrated. For this purpose, the calibrated state could be: every two adjacent antennas have the same phase difference as

$$\phi_{mn} - \phi_{(m-1)n} = \Delta\phi_x, \quad \phi_{mn} - \phi_{m(n-1)} = \Delta\phi_y \quad 2 \le m \le M, \quad 2 \le n \le N. \tag{4}$$

Then ϕ_{mn} can be written as $\phi_{mn} = m\Delta\phi_x + n\Delta\phi_y + \phi_0$, in which ϕ_0 is a scalar initial value. For this calibrated state, Eq. (3) can be rewritten as

$$U(\theta_x, \theta_y) = A(\theta_x, \theta_y) \cdot e^{i\phi_0} \cdot \sum_{m=1}^{M} e^{-im\left(\frac{2\pi}{\lambda} d_x \sin\theta_x - \Delta\phi_x\right)} \cdot \sum_{n=1}^{N} e^{-in\left(\frac{2\pi}{\lambda} d_y \sin\theta_y - \Delta\phi_y\right)} \tag{5}$$

and then we can obtain a clear, distinguishable far-field pattern, as:

$$I(\theta_x, \theta_y) = \left|U(\theta_x, \theta_y)\right|^2 = S(\theta_x, \theta_y) \cdot \frac{\sin M\alpha}{\sin\alpha} \cdot \frac{\sin N\beta}{\sin\beta}, \tag{6}$$

$$S(\theta_x, \theta_y) = \left|A(\theta_x, \theta_y)\right|^2, \quad \alpha = \frac{\pi d_x \sin\theta_x}{\lambda} - \frac{\Delta\phi_x}{2}, \quad \beta = \frac{\pi d_y \sin\theta_y}{\lambda} - \frac{\Delta\phi_y}{2}. \tag{7}$$

Eqs. (6) and (7) show that the far-field pattern follows the form of the Sinc function and depends on two factors: the diffraction factor $S(\theta_x, \theta_y)$ determined by the antenna structure (Fig. 1(b)) and the interference factor that is affected by the arrangement and phase distribution of the antenna

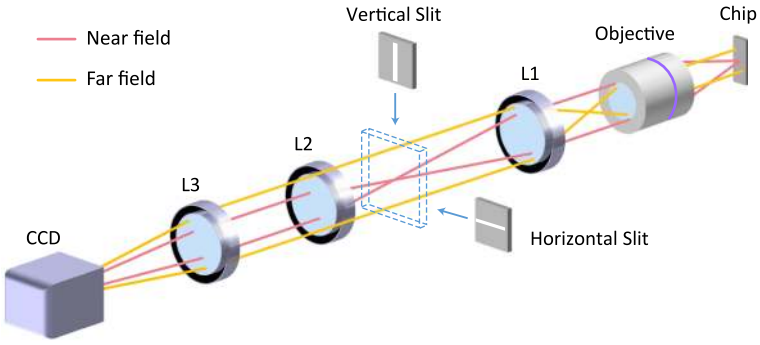

Fig. 3. Schematic of the experimental setup. The near-field and far-field observations are represented as red and yellow ray tracing, respectively, which can be switched by removing Lens2. The objective, L1, L2, and L3 lenses are con-focal and form two relay 4*f* systems.

array. As shown in Fig. 1(c), the diffraction factor (red line) determines the envelope of the far-field pattern. While controlling the phase differences $\Delta\phi_x$ and $\Delta\phi_y$, the main and grating lobes scan together with their peaks following such an envelope. The interference factor defines the range of the field of view (FOV). In addition, the main-lobe position can be tuned by $\Delta\phi_x$ and $\Delta\phi_y$, so we choose the optimal values of $\theta_x = 0^\circ, \theta_y = 8^\circ$ for our design to match the center of diffraction.

The calibrated far-field patterns are shown in Fig. 2(b)–(d). When any two adjacent columns and rows reach the same phase difference, a clear and distinguishable pattern would be realized in the far-field waveform. However, for an incomplete calibration (Fig. 2(e)), the far-field patterns are featured by disordered phase maps and unstable side-lobe power. It is difficult to distinguish these incomplete calibration results from low side-lobe levels. Thus, a more accurate phase calibration is required.

3. Interference-Based Phase Calibration

We hereby propose a phase calibration method from the interference measurement. As schematically shown in Fig. 3, the setup is precisely aligned in a con-focal cage and capable of both near-field and far-field observation.

For the near-field observation, the light emitted from the OPA chip passes through the first 4*f* system consisting of the objective lens (NA = 0.25) and lens L1 ($f_1 = 125$ mm) and the second 4*f* system consisting of lens L2 ($f_1 = 30$ mm) and lens L3 ($f_3 = 10$ mm). Such a two-stage-cascade 4*f* system has 23× magnification for near-field imaging. By removing lens L2, the setup can be switched into the far-field observation and supports a view range of 29°. Placing vertical or horizontal slits at the confocal planes of L1/L2 can block most of the light but allow only the beams of the two adjacent antennas to pass through. During the calibration, we precisely shift the slit to pick up the two-adjacent-antenna emissions in the near field and then switch the setup to the far-field state to observe the interference fringes. The phase difference can be accordingly extracted since the view range has been calibrated through the aperture of the objective lens.

The proposed interference-based calibration was applied on a silicon-based 8 × 8 OPA chip to verify its feasibility. This chip supports an FOV of 8.9° × 2.2°, and the antenna array is uniformly arranged with the spacing $d_x = 10$ μm and $d_y = 40$ μm. The overall footprint of the antenna array is 70 μm × 280 μm. The OPA was operated under TE-polarization in the wavelength of 1550 nm.

The calibration process is presented in detail, as shown in Fig. 4. The emission angle from the single antenna was previously measured as $\theta_x = 0$, $\theta_y = 8^\circ$. We first picked up the emissions from two adjacent antennas in the Y direction (red square), which formed a series of periodic fringes along the θ_y direction. Then we precisely tuned the bias phase of one antenna to make the fringes match with the optimal diffraction direction of $\theta_y = 8^\circ$ and marked it as the red line in Fig. 4(a). So far the first antenna had been calibrated (orange square). Next, the same procedure was utilized to

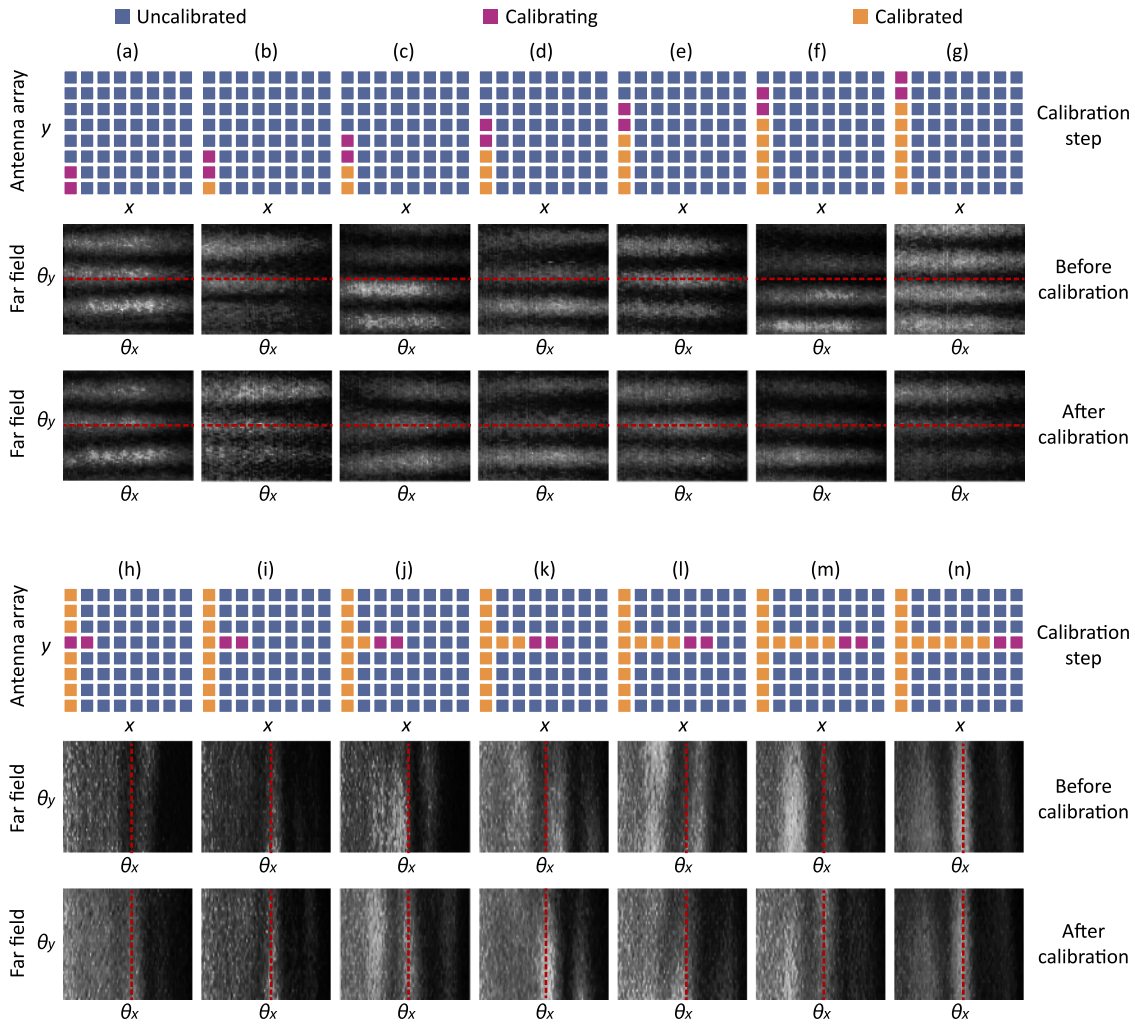

Fig. 4. (a)–(g) The procedure of calibrating the first column of the antenna array. The uncalibrated, calibrating, and calibrated antennas are marked as blue, red, and orange squares (upper panel). Interference fringes are observed in the far-field patterns (middle and lower panel). The bias voltages are tuned to make the bright fringe match with the antenna emission angle $\theta_y = 8^\circ$ (red line). (h)–(n) The row of the antenna array is similarly calibrated to align the bias phases with the antenna emission angle $\theta_x = 0$ (red line).

another two adjacent antennas and progressively repeated across the whole column (Fig. 4(b)–(g)). For each of the antennas, we recorded the bias phase accordingly to build the LUT. After those, the antennas were similarly calibrated in the row manner (Fig. 4(h)–(n)), namely tuning the bias phases to match the optimal diffraction in $\theta_x = 0$ (red line). Repeating the procedure from column to column and row to row, the entire antenna array was calibrated, and the full bias phase map was obtained. Since the two-element interference fringes are brighter and more regular than those side lobes, the proposed calibration method has lower requirements on the feedback sensitivity compared with the algorithm-based calibration methods relied on side-lobe measurement.

Owing to the confocal nature of the cage system, it takes only one minute to calibrate two adjacent antennas each time and costs about one hour for the entire 8 × 8 OPA chip. The process is expected to be automatic in the future for massive productions. The effectiveness of the phase calibration is illustrated in Fig. 5. The near-field pattern with 8 × 8 spots is shown in Fig. 5(a). The far-field patterns, before calibration (Fig. 5(b)) and after (Fig. 5(c)) calibration, are presented for

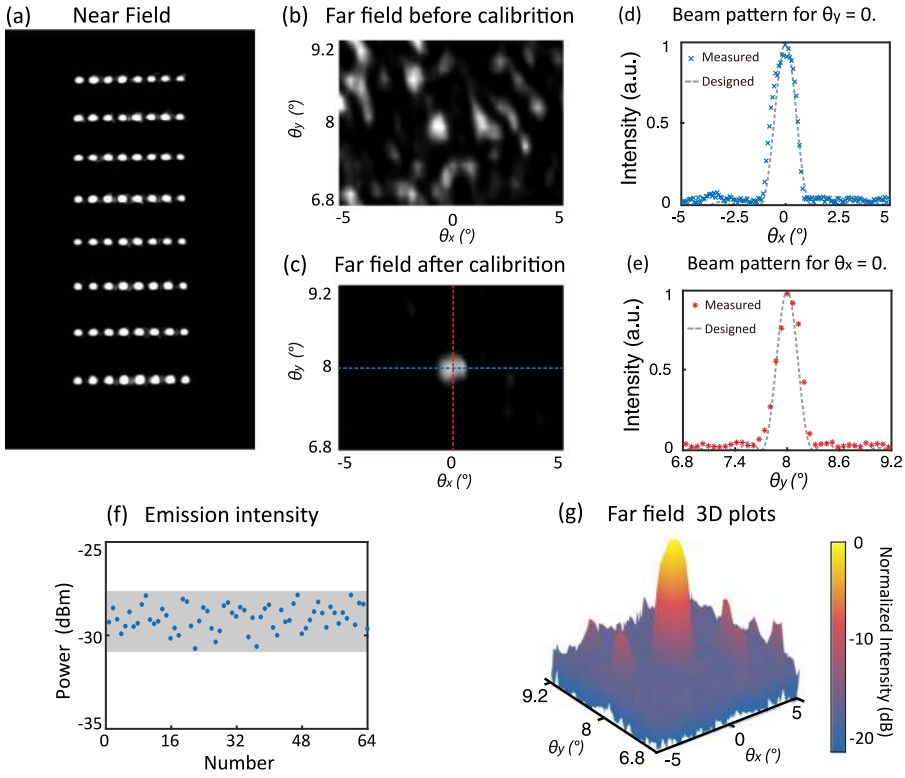

Fig. 5. (a) Near-field pattern of the 8 $\times$ 8 OPA. (b) and (c) are far-field patterns in a full FOV before and after the phase calibration, respectively. (d) and (e) are the sliced far-field pattern in the cross sections of $\theta_y = 0$ and $\theta_x = 0$, respectively. (f) Emission intensity of all of the antennas. The standard deviation of the emission intensity is 0.6 dB. (g) Logarithmic 3D plots of the far-field pattern after phase calibration.

comparison. As shown in Fig. 5(d) and (e), the calibrated far-field pattern has been steered into a divergence angle of $0.92^\circ \times 0.32^\circ$, which agrees well with our design. The emission intensity from each of the antennas is individually measured (Fig. 5(f)). To further characterize the far-field patterns, we convert the intensity distribution into a 3D logarithmic plot (Fig. 5(d)). The side-lobe suppression ratio reaches 10.1 dB owing to the calibration, while without calibration, it was only 1.1 dB. The measured average intensity of one bright fringe is approximately 20 μW/cm^2, which is about 20 times greater than the minimum detectable intensity of our CCD (MicronViewer 7290).

4. Discussion

In order to discuss the feasibility and scalability of the proposed method, we investigated a series of N $\times$ N OPAs where N varies from 2 to 8. In the experiment, the sub-matrices were picked up form an 8 $\times$ 8 OPA chip by using the slits. Their near-field spots are shown in Fig. 6. Still, before the calibration, the far-field patterns are chaotic and indistinguishable (mid panel, Fig. 6). While the calibration was applied, the far-field spots were turned to be distinguishable (lower panel, Fig. 6). In addition, with the scale increasing, the spots become less diverged as expected.

To quantitatively evaluate the calibration effectiveness, we have calculated the side-lobe suppression ratio of the calibrated beams, which was defined as the ratio of intensity between the main lobe and the strongest side lobe in an FOV [37], as shown in Fig. 1(c). The suppression ratios for a series of scales, from both simulation and experiment data, are calculated and presented in Fig. 7. For all of the simulations, the emissions were assumed to be identical in power, but their phases randomly distribute in $[0, 2\pi]$ before calibration. With the random initial phases, the side-lobe suppression

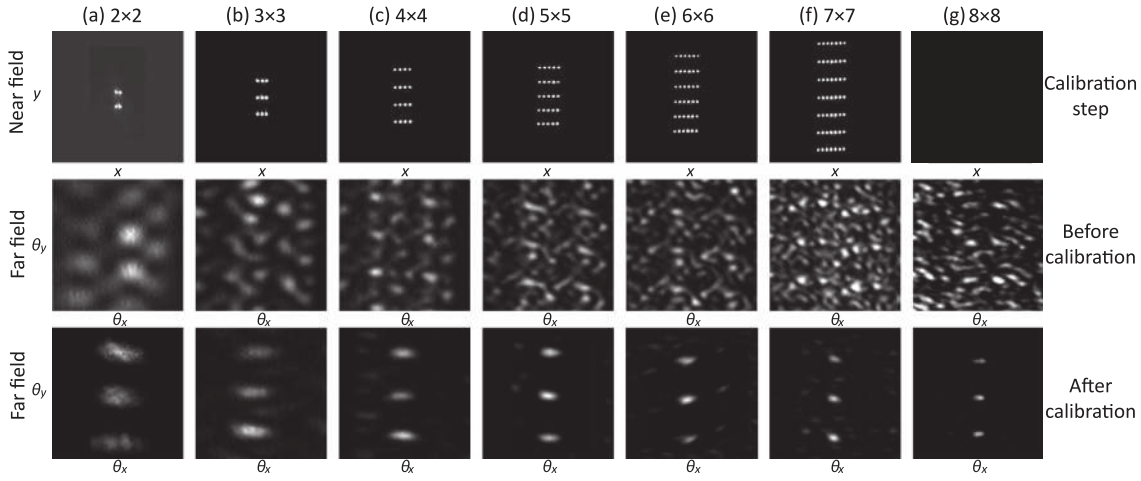

Fig. 6. Near-/far-field patterns of before/after the calibration for N × N arrays, where N varies as (a) 2, (b) 3, (c) 4, (d) 5, (e) 6, (f) 7 and (g) 8.

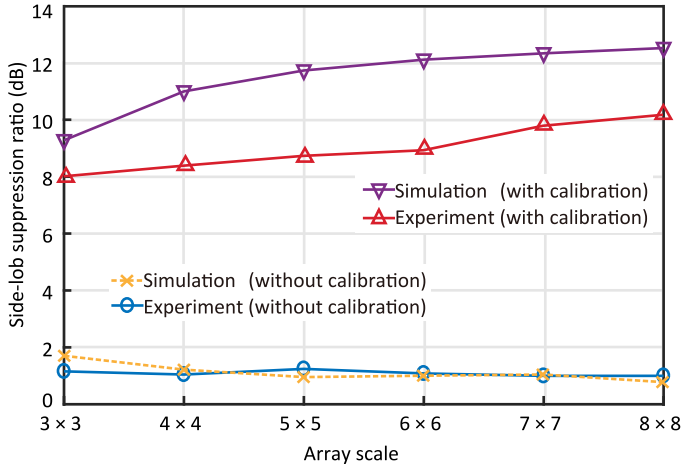

Fig. 7. Side-lobe suppression ratios with different array scales from both simulation and experiment. The blue and red curves are measured from the OPA chip, before and after calibration, respectively. The yellow and purple curves are obtained from the Monte-Carlo simulations.

ratios are almost constant with respect to the scale and kept in poor performance of ∼1 dB. When the phases are calibrated, the side-lobe suppression ratios of approximately 8–10 dB are achieved, which show that the phase calibration is necessary and beneficial.

It is noticed that, there exists ∼2 dB difference in the side-lobe suppression when comparing the simulation and measured results (Fig. 7). The non-uniformity of the emission power (as shown in Fig. 5(f)) is partially responsible for the degrading of the side-lobe suppression. However, it is noteworthy to discuss the influence of the residual phase error, since practically, the limited precision in interference observation can not be ideal.

Here, an analysis of the side-lobe suppression is further presented for the OPAs with different scales, by considering the phase-calibration error $\Delta\phi$ and emission power variation ΔP. As illustrated in Fig. 8, a series of Monte-Carlo simulations have been performed for normal distributed $\Delta\phi$ with given standard deviations. More specifically, a set of phase and power errors are randomly generated, which follows a normal distribution $N(\Delta\phi, \Delta P)$, and then the side-lobe suppression ratios are calculated accordingly. This procedure is repeated 100 times from the same given

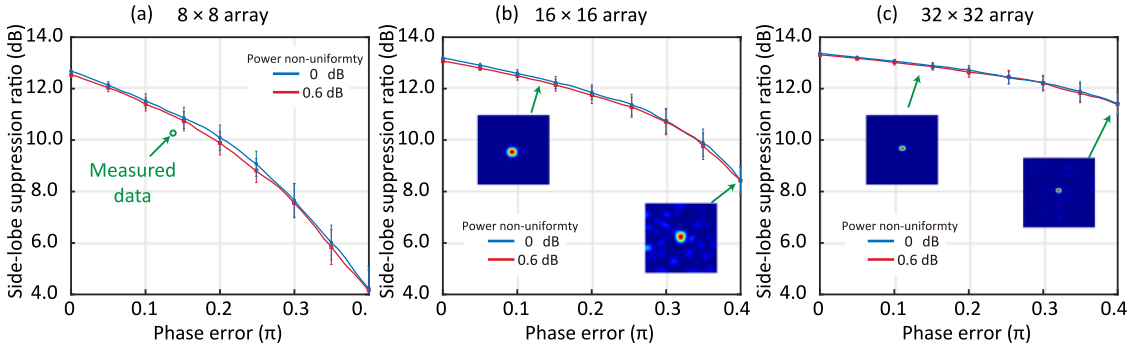

Fig. 8. Monte-Carlo simulations of the side-lobe suppression ratios affected by residual calibration phase errors and the emission power non-uniformity. The standard deviation of the phase error and power is assumed as 0–0.4π and 0.6 dB, respectively. The array scales of N $\times$ N are investigated, where N = 8, 16 and 32.

$N(\Delta\phi, \Delta P)$ as Monte-Carlo runs. The assembly statistical results are presented for the scale of 8 $\times$ 8, 16 $\times$ 16, and 32 $\times$ 32, respectively.

For the 8 $\times$ 8 OPA (the case of our experimental observation), the measured standard deviation of the residual phase error is 0.13π by analyzing the interference data. Actually, the camera used in the experiment captures one bright fringe by using $\sim$16 pixels. Given the measurement uncertainty of 2 pixels, namely the phase uncertainty is about $1/8\pi$ which is quite close to estimate value of 0.13π. Meanwhile, according to the side-lob suppression degrading of $\sim$2 dB from the perfectly calibrated case, the phase-calibration error of 1.3π is within a reasonable range considering the optical noise. It is also noticed from Fig. 8 that, the power non-uniformity shows quite limit impact on the side-lobe suppression. Therefore, it can be concluded that the difference in simulated and measured side-lobe suppression (Fig. 7) is mainly induced by the phase-calibration error. It is not counter-intuitive that, with increasing the array scale, the side-lobe suppression are then less sensitive to the phase-calibration error, as shown in Fig. 8. Therefore, the larger-scale OPAs would be practically easier for the calibration.

We note that the waveguide spacing in our design is sufficiently large, so that the thermal cross-talks between adjacent channels are negligible. The calibration errors mainly come from the matching error in extracting the fringe peaks, while it can be optimized by increasing the magnification or applying more sophisticated image processing algorithms upon the interference fringes.

5. Conclusion

In this work, an interference-based technique is proposed and demonstrated to physically calibrate the randomly distributed initial phases of on-chip OPAs to generate clear and stared beam patterns. Specifically, we extract the phase difference between two adjacent antenna emissions from their interference fringes, and progressively repeat this procedure in a column-to-column and row-to-row manner. After all, the phase map of the entire antenna array is obtained for the operation of OPAs.

The feasibility and effectiveness of the proposed calibration method is verified by an silicon-based 8 $\times$ 8 OPA sample. The side-lobe suppression of 10.1 dB is achieved, and the impacts of the emission power non-uniformity and the residual phase error are discussed. The results show that the phase error is the dominate reason in deteriorating the far-field patterns, and thus, an accurate phase calibration is indispensable for high-performance OPAs.

Comparing with those conventional calibration methods, most of which are performed by algorithms, the proposed method is physical and has lower requirements on feedback systems. The interference-based phase calibration can be combined with conventional algorithms to provide a

well-defined solution candidate letting algorithm optimization avoid local optima, thus could be beneficial for practical OPA applications.

Appendix: Detailed Parameters of the OPA Chip

	Parameter	Value
OPA system	SOI wafer	220 nm Si / 2 μm SiO_2 box
	system scale	$8 \times 8 = 64$
	antenna array footprint	70 μm × 280 μm
	Incident wavelength λ	1550 nm
	Main-lobe width (calculated)	$0.98^\circ \times 0.25^\circ$
	Main-lobe width (measured)	$0.92^\circ \times 0.32^\circ$
	Scanning range	$8.9^\circ \times 2.2^\circ$
	Side-lobe suppression ratio (before calibration)	1.1 dB
	Side-lobe suppression ratio (after calibration)	10.1 dB
EO phase shifter	Waveguide rib width	600 nm
	Waveguide rib height	130 nm
	Waveguide slab width	1.6 μm
	Waveguide slab hight	90 μm
	Material, P++ doping density	Boron, $10^{20}/cm^3$
	Material, N++ doping density	Phosphorus, $10^{20}/cm^3$
	$0 - 2\pi$ Bias voltage	0.85 V to 1.2 V
Antenna	Emission direction	$0^\circ \times 8^\circ$
	Emission range	$18^\circ \times 24^\circ$
	Insertion loss	4.5 dB to 6 dB
Drive circuits	Output voltage range	0 V to 2.4 V
	Channel number	64
	Output voltage resolution	0.004 V
	Drive capability	100 mA/V

References

[1] P. F. McManamon *et al.*, "Optical phased array technology," *Proc. IEEE*, vol. 84, no. 2, pp. 268–298, Feb. 1996.
[2] M. K. Smit, "New focusing and dispersive planar component based on an optical phased array," *Electron. Lett.*, vol. 24, no. 7, pp. 385–386, 1988.
[3] K. Van Acoleyen, W. Bogaerts, J. Jágerská, N. Le Thomas, R. Houdré, and R. Baets, "Off-chip beam steering with a one-dimensional optical phased array on Silicon-on-insulator," *Opt. Lett.*, vol. 34, no. 9, pp. 1477–1479, 2009.
[4] J. J. López *et al.*, "Planar-lens enabled beam steering for chip-scale LIDAR," in *Proc. IEEE Conf. Lasers Electro-Opt.*, 2018, pp. 1–2.
[5] S. Chung, H. Abediasl, and H. Hashemi, "A monolithically integrated large-scale optical phased array in Silicon-on-insulator CMOS," *IEEE J. Solid-State Circuits*, vol. 53, no. 1, pp. 275–296, Jan. 2018.
[6] J. Sun, E. Timurdogan, A. Yaacobi, E. S. Hosseini, and M. R. Watts, "Large-scale nanophotonic phased array," *Nature*, vol. 493, no. 7431, 2013, Art. no. 195.
[7] M. Raval, A. Yaacobi, and M. R. Watts, "Integrated visible light phased array system for autostereoscopic image projection," *Opt. Lett.*, vol. 43, no. 15, pp. 3678–3681, 2018.
[8] T. Su, R. P. Scott, S. S. Djordjevic, N. K. Fontaine, D. J. Geisler, X. Cai, and S. Yoo, "Demonstration of free space coherent optical communication using integrated silicon photonic orbital angular momentum devices," *Opt. Express*, vol. 20, no. 9, pp. 9396–9402, 2012.

[9] D. Resler, D. Hobbs, R. Sharp, L. Friedman, and T. Dorschner, "High-efficiency liquid-crystal optical phased-array beam steering," *Opt. Lett.*, vol. 21, no. 9, pp. 689–691, 1996.
[10] X. Wang, B. Wang, P. J. Bos, P. F. McManamon, J. J. Pouch, F. A. Miranda, and J. E. Anderson, "Modeling and design of an optimized liquid-crystal optical phased array," *J. Appl. Phys.*, vol. 98, no. 7, 2005, Art. no. 073101.
[11] D. Engström, M. J. O'Callaghan, C. Walker, and M. A. Handschy, "Fast beam steering with a ferroelectric-liquid-crystal optical phased array," *Appl. Opt.*, vol. 48, no. 9, pp. 1721–1726, 2009.
[12] B. Wang, G. Zhang, A. Glushchenko, J. L. West, P. J. Bos, and P. F. McManamon, "Stressed liquid-crystal optical phased array for fast tip-tilt wavefront correction," *Appl. Opt.*, vol. 44, no. 36, pp. 7754–7759, 2005.
[13] B.-W. Yoo *et al.*, "A 32 $\times$ 32 optical phased array using polysilicon sub-wavelength high-contrast-grating mirrors," *Opt. Express*, vol. 22, no. 16, pp. 19 029–19 039, 2014.
[14] T. K. Chan *et al.*, "Optical beamsteering using an 8 $\times$ 8 mems phased array with closed-loop interferometric phase control," *Opt. Express*, vol. 21, no. 3, pp. 2807–2815, 2013.
[15] J.-D. Shin, B.-S. Lee, and B.-G. Kim, "Optical true time-delay feeder for x-band phased array antennas composed of 2/spl times/2 optical mems switches and fiber delay lines," *IEEE Photon. Technol. Lett.*, vol. 16, no. 5, pp. 1364–1366, May 2004.
[16] S. T. Fryslie, M. T. Johnson, and K. D. Choquette, "Coherence tuning in optically coupled phased vertical cavity laser arrays," *IEEE J. Quantum Electron.*, vol. 51, no. 11, Nov. 2015, Art. no. 2600206.
[17] T. Shay *et al.*, "First experimental demonstration of self-synchronous phase locking of an optical array," *Opt. Express*, vol. 14, no. 25, pp. 12 015–12 021, 2006.
[18] E. Bochove, P. Cheo, and G. King, "Self-organization in a multicore fiber laser array," *Opt. Lett.*, vol. 28, no. 14, pp. 1200–1202, 2003.
[19] K. Sayyah *et al.*, "Two-dimensional pseudo-random optical phased array based on tandem optical injection locking of vertical cavity surface emitting lasers," *Opt. Express*, vol. 23, no. 15, pp. 19 405–19 416, 2015.
[20] J. Sun *et al.*, "Large-scale Silicon photonic circuits for optical phased arrays," *IEEE J. Sel. Topics Quantum Electron.*, vol. 20, no. 4, Jul./Aug. 2014, Art. no. 8201115.
[21] J. Sun *et al.*, "Two-dimensional apodized Silicon photonic phased arrays," *Opt. Lett.*, vol. 39, no. 2, pp. 367–370, 2014.
[22] J. Sun, M. Moresco, G. Leake, D. Coolbaugh, and M. R. Watts, "Generating and identifying optical orbital angular momentum with silicon photonic circuits," *Opt. Lett.*, vol. 39, no. 20, pp. 5977–5980, 2014.
[23] J. K. Doylend, M. Heck, J. T. Bovington, J. D. Peters, L. Coldren, and J. Bowers, "Two-dimensional free-space beam steering with an optical phased array on Silicon-on-insulator," *Opt. Express*, vol. 19, no. 22, pp. 21 595–21 604, 2011.
[24] J. Hulme *et al.*, "Fully integrated hybrid silicon two dimensional beam scanner," *Opt. Express*, vol. 23, no. 5, pp. 5861–5874, 2015.
[25] K. Van Acoleyen, H. Rogier, and R. Baets, "Two-dimensional optical phased array antenna on Silicon-on-insulator," *Opt. Express*, vol. 18, no. 13, pp. 13 655–13 660, 2010.
[26] K. Van Acoleyen, W. Bogaerts, and R. Baets, "Two-dimensional dispersive off-chip beam scanner fabricated on silicon-on-insulator," *IEEE Photon. Technol. Lett.*, vol. 23, no. 17, pp. 1270–1272, Sep. 2011.
[27] C. V. Poulton *et al.*, "Coherent solid-state lidar with silicon photonic optical phased arrays," *Opt. Lett.*, vol. 42, no. 20, pp. 4091–4094, 2017.
[28] C. V. Poulton, *et al.*, "Long-range LiDAR and free-space data communication with high-performance optical phased arrays," *IEEE J. Sel. Topics Quantum Electron.*, vol. 25, no. 5, Sep./Oct. 2019, Art. no. 7700108.
[29] B. Abiri, R. Fatemi, and A. Hajimiri, "A 1-D heterodyne lens-free optical phased array camera with reference phase shifting," *IEEE Photon. J.*, vol. 10, no. 5, Oct. 2018, Art. no. 6601712.
[30] T. Komljenovic, R. Helkey, L. Coldren, and J. E. Bowers, "Sparse aperiodic arrays for optical beam forming and LIDAR," *Opt. Express*, vol. 25, no. 3, pp. 2511–2528, 2017.
[31] F. Aflatouni, B. Abiri, A. Rekhi, and A. Hajimiri, "Nanophotonic projection system," *Opt. Express*, vol. 23, no. 16, pp. 21 012–21 022, 2015.
[32] D. N. Hutchison *et al.*, "High-resolution aliasing-free optical beam steering," *Optica*, vol. 3, no. 8, pp. 887–890, 2016.
[33] J. L. M. Fuentes, E. J. Fernández, P. M. Prieto, and P. Artal, "Interferometric method for phase calibration in liquid crystal spatial light modulators using a self-generated diffraction-grating," *Opt. Express*, vol. 24, no. 13, pp. 14 159–14 171, 2016.
[34] F. Xiao, L. Kong, and J. Chen, "Beam-steering efficiency optimization method based on a rapid-search algorithm for liquid crystal optical phased array," *Appl. Opt.*, vol. 56, no. 16, pp. 4585–4590, 2017.
[35] T. Komljenovic and P. Pintus, "On-chip calibration and control of optical phased arrays," *Opt. Express*, vol. 26, no. 3, pp. 3199–3210, 2018.
[36] L.-J. Li, W. Chen, X.-Y. Zhao, and M.-J. Sun, "Fast optical phased array calibration technique for random phase modulation LiDAR," *IEEE Photon. J.*, vol. 11, no. 1, Feb. 2019, Art. no. 6900410.
[37] R. Fatemi, A. Khachaturian, and A. Hajimiri, "A nonuniform sparse 2-D large-FOV optical phased array with a low-power PWM drive," *IEEE J. Solid-State Circuits*, vol. 54, no. 5, pp. 1200–1215, May 2019.